Article

Data-Driven Modelling of TEHL Contacts: ANN-Based Prediction of Friction, Film Thickness, and Temperature

Peyman Havaej [1,†,‡*] and Dieter Fauconnier [2,‡]

[1] Soete Laboratory, Department of Electromechanical, Systems & Metal Engineering, Faculty of Engineering and Architecture, Ghent University; peyman.havaej@ugent.be
[2] Flanders Make @ UGent – Core Lab MIRO
* Correspondence: peyman.havaej@ugent.be

Abstract: Conventional Thermo-Elastohydrodynamic Lubrication (TEHL) simulations, while accurate, are computationally expensive and impractical for system-level analyses. In this study, Artificial Neural Network (ANN)-based surrogate models were developed for predicting key TEHL outputs, including Coefficient of Friction (CoF), rolling friction, maximum temperature, and film thickness metrics. A comprehensive dataset of approximately 36,000 samples was generated by solving the generalised Reynolds equation and Boussinesq integral under non-Newtonian and non-isothermal conditions, capturing thermal effects that are often neglected in previous studies, particularly for friction prediction. Separate ANN models were trained for each output while hyperparameters were optimized, achieving high predictive accuracy with R^2 values exceeding 0.99 for most outputs. To address data sparsity and improve, particularly, the CoF prediction, a novel adaptive sampling strategy was implemented, enriching low-density regions of the output space and enhancing generalisation and accuracy. Sensitivity analysis revealed that CoF is primarily influenced by the piezo-viscous coefficient and Slide-to-Roll Ratio (SRR), while film thickness metrics depend on entrainment speed and viscosity. Moreover, maximum temperature rise is dominated by SRR and pressure-viscosity effects, with thermal properties playing a minor role for most of the TEHL outputs. The proposed models demonstrate good agreement with reference TEHL solutions across diverse operating conditions, offering a computationally efficient alternative for real-time calculations of lubricated contacts.

Keywords: Thermo-Elastohydrodynamic Lubrication (TEHL), Coefficient of Friction (CoF), Rolling Friction, Film Thickness Prediction, Machine Learning, Artificial Neural Networks (ANN), Surrogate Modelling

1. Introduction

TEHL is a lubrication regime that occurs in machine components such as gears, rolling element bearings, and cam–follower systems, where both elastic deformation of the contacting bodies and thermal effects strongly influence behaviour. The key parameters of interest in TEHL include lubricant film thickness, contact stresses, temperature distributions, and friction levels, as these govern wear, efficiency, and ultimately component lifetime. Predicting these quantities with sufficient accuracy is critical to ensuring the reliability and performance of machines. However, TEHL contact problems-though already studied for decades using different modelling techniques-are in essence notoriously complex and computationally intensive to solve, due to the strong multi-physics coupling between fluid dynamics, solid deformation and the highly complex constitutive behaviour of the lubricant under the governing contact conditions. Integrating comprehensive TEHL simulations into component or system-level calculations, where multiple contacts interact under different and time-varying conditions and nested-iterative solution algorithms are required, is currently prohibitive with conventional methods.

Existing approaches to modelling TEHL can be viewed along a spectrum of computational cost versus accuracy and completeness of the physical description. At one end, full-order modelling based on computational fluid dynamics solves the full Navier–Stokes and energy conservation equations, coupled with elasticity to capture surface deformation. This provides the most detailed representation of the pressure, temperature, and stress fields within a lubricated contact and is unrivalled in terms of reliability and accuracy. However, such simulations are very costly, often requiring days to complete a single case, and therefore most suitable for in-depth academic studies [1].

Lower-dimensional (reduced-order) models, such as the Reynolds equation, offer a more computationally tractable alternative by simplifying the Navier–Stokes momentum equations for thin lubricant films. These models are coupled with elastic deformation models through fully coupled solvers [2], semi-coupled schemes [3], or partitioned methods accelerated by multi-grid techniques [4]. Such approaches can reduce computation time from days to minutes, and they have been validated against experiments [5,6]. Despite these advantages, their repeated use in higher-level simulations—such as component-scale or multi-body dynamics models—remains computationally demanding. To mitigate this limitation, various Model Order Reduction (MOR) techniques have been proposed. Habchi and Issa [7] applied MOR to the elastic domain only, using static condensation to reduce the number of solid degrees of freedom, achieving 15 times acceleration without considerably compromising the solution fidelity. In contrast, Scurria et al. [8] proposed a full-domain reduction strategy, combining Galerkin projection for the solid domain with hyper-reduction of the Reynolds equation, enabling up to three orders of magnitude in computational speedup for Newtonian and isothermal Elastohydrodynamic Lubrication (EHL) problems.

Finally, surrogate models, of which analytical models are well-known and widely used, provide closed-form or semi-empirical estimates of key parameters, mainly limited to central or minimum film thickness. Formulations include those of Dowson and Higginson [9] and Moes [10]. These are in essence all fittings to pure EHL solutions, historically generated using Reynolds-based reduced order models, assuming steady-state, pure rolling, isothermal, Newtonian conditions. in time, corrections have been introduced to extend these expressions to wider operating conditions, including inlet shear heating [11], non-Newtonian effects [12], and lubricant compressibility [13]. While computationally efficient, the applicability of classic analytical models is often limited by the assumptions underlying their derivation and/or by compatibility issues between different correction factors. This limits their generalisation to rolling–sliding, non-isothermal, and non-Newtonian TEHL problems.

Furthermore, while film thickness has traditionally been the primary focus of analytical approaches, other outputs such as the CoF, maximum contact temperature, and rolling friction are equally critical for engineering applications in view of system-level simulations. Analytical formulations for these quantities are, however, often oversimplified. For example, expressions for the CoF, such as those proposed by Gupta [14], typically rely on restrictive constitutive assumptions. Similarly, predictions of rolling friction, such as those presented by Houpert [15], have been shown to deviate significantly from experimental observations [16]. These limitations restrict the utility of classical analytical models when a broader set of contact performance metrics is required.

With the growing availability of computational resources, the expansion of high-fidelity simulation datasets, and the increasing demand for real-time predictive tools, Machine Learning (ML) has emerged as a promising complement or alternative to conventional TEHL modelling. ML frameworks are capable of capturing the complex, nonlinear relationships governing lubricated contacts without requiring explicit physical simplifications.

Habchi and Bair [17] investigated the influence of high-pressure lubricant rheology on the formation of minimum film thickness in EHL circular contacts. Challenging the traditional focus on low-pressure inlet rheology, they employed a ML model based on Gaussian Process Regression (GPR). Under the assumption of steady-state, isothermal, Newtonian contacts with hypothetical fluids that shared identical low-pressure responses but differed in high-pressure behaviour, they demonstrated that conventional dimensionless parameters are inadequate for characterising the minimum film

thickness. Instead, they highlighted the need to incorporate an additional pressure-viscosity coefficient—evaluated at half the Hertzian contact pressure—for accurate prediction. While GPR can provide accurate fits for small or limited datasets, it may exhibit reduced generalisation and higher sensitivity to noise when applied to unseen data, particularly compared to ANN, which can better capture complex patterns in larger datasets. In a related effort to advance data-driven modelling in tribology, Walker et al. [18] employed ANN to efficiently predict key parameters such as central film thickness and friction in lubricated contacts under the isothermal assumption. Their model's predictions were compared against experimental ball-on-disk measurements.

Singh et al. [19] further demonstrated the capabilities of ANN by predicting maximum temperature in TEHL line contacts, achieving an accuracy of $R^2 = 0.997$ using only two hidden layers in their Neural Network. They also examined the effects of varying network structure and input feature selection, although the features were limited to subsets of existing dimensional parameters. Extending ANN applications to more complex contact geometries, Tosic et al. [20] focused on predicting film thickness in elliptical contacts with varying lubricant entrainment angles relevant to worm gear systems. They optimised network architecture, validation data splits, and backpropagation algorithms to achieve high accuracy with low bias and variance, using a limited dataset of 691 points. Reinforcing the versatility of ANN-based approaches, Kelly et al. [21] developed a model for localised prediction of pressure and film thickness in EHL line contacts. Compared to simplified analytical models, their ANN provided more accurate estimates of film thickness, rolling and sliding friction, and electrical capacitance, all with errors below 5 %. However, the dataset was generated under isothermal conditions, which significantly affects the accuracy of sliding friction predictions. Nonetheless, their work underscores the potential for neural networks to replace curve-fitted models in large-scale tribological simulations, enabling more detailed physical modelling without the computational burden.

While many studies have focused on predicting film thickness using ML algorithms, far less attention has been given to predicting the CoF and rolling friction—despite their central role in quantifying load-dependent power losses in lubricated machine elements. Existing research on CoF has considered isothermal conditions, overlooking the non-negligible influence of temperature on friction. Accurate prediction of these load-dependent losses is crucial for estimating power losses in components such as bearings and spur gears in system-level simulations.

This study introduces a framework for predictive modelling of TEHL line contacts using ANN, enabling accurate estimation of CoF, rolling friction, maximum temperature, and film thickness metrics. The training dataset is generated from Reynolds-Boussinesq TEHL simulation across a wide range of operating conditions, incorporating non-Newtonian and thermal effects, an aspect neglected in previous surrogate modelling studies for friction prediction. To enhance model robustness, outlier detection is applied to filter numerical artifacts by combining two different methods to detect local and global outliers. Crucially, this work introduces an adaptive sampling strategy—a new contribution in the context of TEHL surrogate modelling—which systematically enriches sparse regions of the output space. This targeted data augmentation improves CoF prediction, particularly in critical regions of the traction curve where the original sample distribution exhibits greater deviation from the reference solution. Sensitivity analyses further reveal the dominant influence of operating conditions and lubricant properties on tribological outputs, supporting model interpretability. The resulting surrogate models achieve high accuracy and computational efficiency, enabling real-time estimation of tribological behaviour, system-level power losses, and lubrication conditions.

2. Method

The following section outlines the governing equations used for TEHL line contact modelling and the numerical algorithm employed to solve them. Subsequently, the architecture of the ML model is presented and discussed in detail.

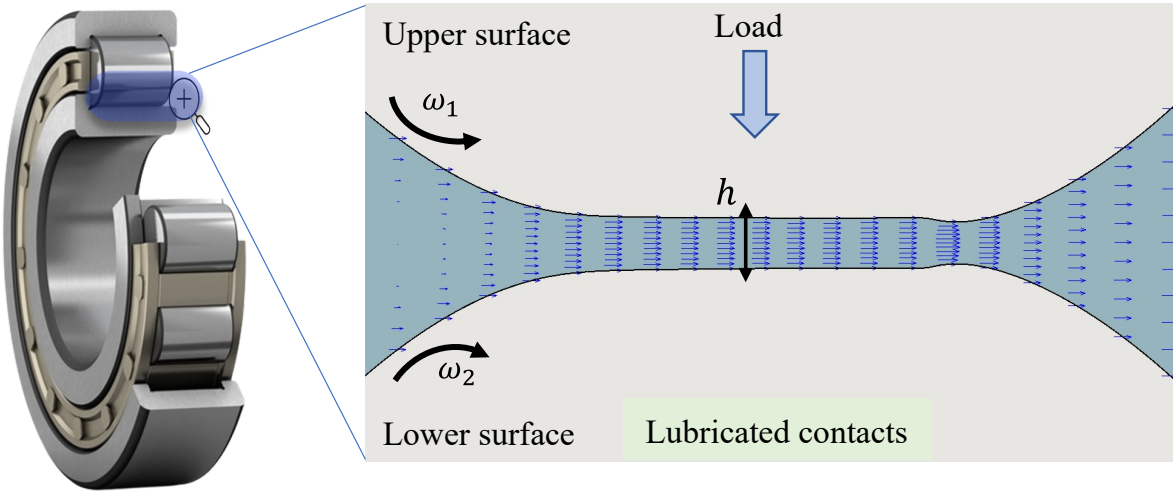

Figure 1. A schematic of a TEHL contact observed in bearings.

2.1. TEHL equations

The contact simulation in this study was performed by solving the Reynolds equation for flow and the Boussinesq integral for surface deformation. For a TEHL line contact, the pressure can be calculated from the following equation [22]:

$$\frac{\partial}{\partial X}\left(\bar{\varepsilon}\frac{\partial P}{\partial X}\right) = \frac{\partial(\bar{\rho}_x^* \theta H)}{\partial X} \tag{1}$$

where:

$$\begin{aligned} &\bar{\varepsilon} = \frac{H^3 p_h a_H^3}{u_m \eta_R R_{eq}^2}\left(\frac{\bar{\eta}_e}{\bar{\eta}_e'}\bar{\rho}' - \bar{\rho}''\right) \\ &\text{with } \bar{\rho}' = \int_0^1 \bar{\rho}\int_0^Z \frac{dZ'}{\bar{\eta}}dZ \quad \text{and} \quad \bar{\rho}'' = \int_0^1 \bar{\rho}\int_0^Z \frac{Z'dZ'}{\bar{\eta}}dZ \\ &\frac{1}{\bar{\eta}_e} = \int_0^1 \frac{dZ}{\bar{\eta}}, \quad \frac{1}{\bar{\eta}_e'} = \int_0^1 \frac{ZdZ}{\bar{\eta}}, \quad \bar{\rho}_x^* = \frac{\bar{\rho}_e u_1 + \bar{\eta}_e u_s \bar{\rho}'}{u_m} \text{ and } \bar{\rho}_e = \int_0^1 \bar{\rho}dZ \end{aligned} \tag{2}$$

Non-dimensional quantities are defined as

$$X = \frac{x}{a_H}, Z = \frac{z}{h}, P = \frac{p}{P_H}, H = \frac{hR_{eq}}{a_H^2}, \eta^* = \frac{\eta}{\eta_R}, \rho^* = \frac{\rho}{\rho_R} \tag{3}$$

After obtaining the pressure, the velocity field is determined as below

$$u_f = u_1 + \frac{p_H H^2 a_H^3}{\eta_R R_{eq}^2}\frac{\partial P}{\partial X}\left[\int_0^Z \frac{Z'\,dZ'}{\bar{\eta}} - \frac{\bar{\eta}_e}{\bar{\eta}'}\int_0^Z \frac{dZ'}{\bar{\eta}}\right] + \bar{\eta}_e u_s \int_0^Z \frac{dZ'}{\bar{\eta}} \tag{4}$$

Assuming a smooth surface, the film thickness can be obtained from:

$$H(X) = H_0(t) + \frac{X^2}{2} + \overline{D}(X) \tag{5}$$

where $\overline{D}$ is the deformation in non-dimensional form that can be read from:

$$\overline{D}(X) = -\frac{1}{2\pi}\int_{X_{\min}}^{X_{\max}} P(S)\ln(X-S)^2 dS \tag{6}$$

which is based on the Boussinesq integral for surface deformation for a line contact [23].

For precise predictions of friction and film thickness, temperature effects must be taken into account. Hence, the following energy equation is being solved along with the pressure and deformation equations [24].

$$\nabla \cdot (\rho c_p u T) - \rho u T \frac{\partial C_p}{\partial x} = \nabla \cdot (k \nabla T) + \beta_T T \left(u \frac{\partial p}{\partial x} \right) + \eta \left(\frac{\partial u}{\partial z} \right)^2 \tag{7}$$

In this equation, the viscous heating and compressive work on the lubricant are considered as source terms. Moreover, the Carslaw-Jaeger thermal condition is imposed for the moving surfaces to predict the temperature field on the surfaces for a steady-state condition. This boundary condition as follows [25,26]:

$$T_{CJ} = T_0 + \sqrt{\frac{1}{\pi \rho_s C_{p,s} k_s u_s}} \int_{-\infty}^{x} q_f(\hat{x}) \frac{d\hat{x}}{\sqrt{x - \hat{x}}} \tag{8}$$

The surface temperature is influenced by both the thermal properties of the solid and its rotating speed. The Carslaw–Jaeger condition is applicable when the Peclet number ($Pe = \frac{u_s l_{ch}}{k_s / (\rho_s C_{p,s})}$) is greater than 5 at the surface. Additional details and related equations can be found in [1,26].

For the constitutive modelling of the lubricant, the Dowson density model, along with the Roelands-Houpert Newtonian viscosity, and the Eyring model for the shear-thinning effects, are employed. They can be calculated as follows:

Dowson density equation:

$$\rho = \rho_R \left(\frac{5.9 \times 10^8 + 1.34p}{5.9 \times 10^8 + p} \right) [1 - \beta_T (T - T_R)] \tag{9}$$

Roelands-Houpert viscosity equation [27]:

$$\mu_{Roelands} = \mu_R exp \left\{ (ln(\mu_R) + 9.67) \left(\left[1 + \frac{p}{p_{r,0}} \right]^z - 1 \right) \left(\frac{T - 138}{T_R - 138} \right)^{-\frac{\beta (T_R - 138)}{ln(\mu_R) + 9.67}} \right\} \tag{10}$$

$$\mu_{RH} = \mu_{Roelands} exp(-\beta^* (T - T_R)) \tag{11}$$

Eyring shear thinning model

$$\eta(p,\ T,\ \dot{\gamma}) = \frac{\tau_0}{\dot{\gamma}} sinh^{-1} \left(\frac{\mu_{RH} \dot{\gamma}}{\tau_0} \right) \tag{12}$$

For simplicity and to reduce the number of parameters during subsequent training with the ANN model, it is assumed that thermal properties remain constant and independent of pressure and temperature. It is acknowledged that this assumption may affect the accuracy of the TEHL solution [28]. The Dowson, Roelands-Houpert, and Eyring models are selected for their straightforward physical interpretation and ease of defining parameter ranges. More complex (and potentially more accurate) models, such as the Tait, Doolittle, and Carreau models, are more cumbersome for parameter estimation, making them less practical for this study, which focuses on ANN development.

In this study, the shear component of the resistive forces is referred to as the CoF, and it is computed at the lower surface as below:

$$CoF = \frac{F_\tau}{F} = \frac{\int \overrightarrow{\tau_w} . \overrightarrow{e_t} dA}{\int p . \overrightarrow{e_n} dA} \tag{13}$$

The second resistive force considered is rolling friction. This arises due to the asymmetry in the pressure distribution, where the pressure centre is slightly shifted toward the inlet of the contact. This

Algorithm 1 TEHL Solver Algorithm

1: **for** itr $= 1$ to $\text{itr}_{\max}$ **do**
2: Solve pressure and Lubricant film fraction (p and θ)
3: Update film thickness (H)
4: Update lubricant properties (ρ, μ, k, C_p, and integrals in Equation (2))
5: Update H_0 based on load balance
6: Solve energy equation every n (=25) iterations (T)
7: Check convergence for load, film thickness, and temperature ($\Delta F < \epsilon_F$, $\Delta H < \epsilon_H$, and $\Delta T < \epsilon_T$)
8: **end for**
9: Post-processing results

offset generates an additional torque that resists the rolling motion of the surfaces. The rolling friction force and pressure eccentricity are calculated as follows [16]:

$$F_{roll} = \frac{\int p \cdot x \cdot dx}{R_{eq}}, \; e_p \quad = \frac{\int p \cdot x \cdot dx}{F}, \tag{14}$$

where x denotes the distance from the centre of the contact, and F represents the hydrodynamic force, defined as the total normal force resulting from pressure acting on the surface. It is important to note that in a one-dimensional line contact simulation, F_{roll} has units of N/m, while e_p is expressed in m. In the subsequent sections, the normalised rolling friction force is represented as:

$$F_R = \frac{F_{roll}}{R_{eq}}, \tag{15}$$

which provides a consistent analogy with the CoF.

2.2. TEHL numerical algorithm

The numerical algorithm of the TEHL solver is briefly presented in Algorithm 1. The Partial Differential Equations (PDEs) are discretised on the uniform mesh using Finite Volume Method (FVM). The semi-system approach has been implemented here for pressure-deformation coupling. In this method, the Couette term in the discretised Reynolds equation is reformulated as a function of pressure by substituting the discretised form of the Boussinesq integral from Equation (6) into the film thickness expression in Equation (5). This yields:

$$H_i = H_0 + \frac{X_i^2}{2} + \sum_{j=1}^{M} K_i^j P_j, \tag{16}$$

where K_i^j are influence coefficients representing the elastic deformation at node i due to a unit pressure at node j. Incorporating these terms into the system matrix modifies the coefficients of the tridiagonal system, thereby increasing diagonal dominance. This restructuring improves numerical stability and accelerates convergence, particularly under heavily loaded or starved conditions where the Poiseuille contribution is small or negligible [3,29].

The well-known PETSc package [30,31] has been used to solve the sparse matrix after discretisation of the pressure and temperature equations. Additionally, the Fast Fourier Transform (FFT) has been utilised to accelerate the calculations of surface deformation [32]. Note that each numerical simulation typically takes 1 min to 5 min, depending on operating condition, utilising an AMD EPYC 7F72 24-Core Processor, each operating at a frequency of 3.6 GHz.

The tolerances mentioned in Algorithm 1 are considered as 1×10^{-6}, 1×10^{-5}, and 1×10^{-5} for mutual approach, load balance, and temperature, respectively. The relative error is used for load balance and temperature. Such strong convergence criteria are essential as the TEHL simulations will be conducted on a wide range of parameters. Moreover, to accelerate convergence and improve

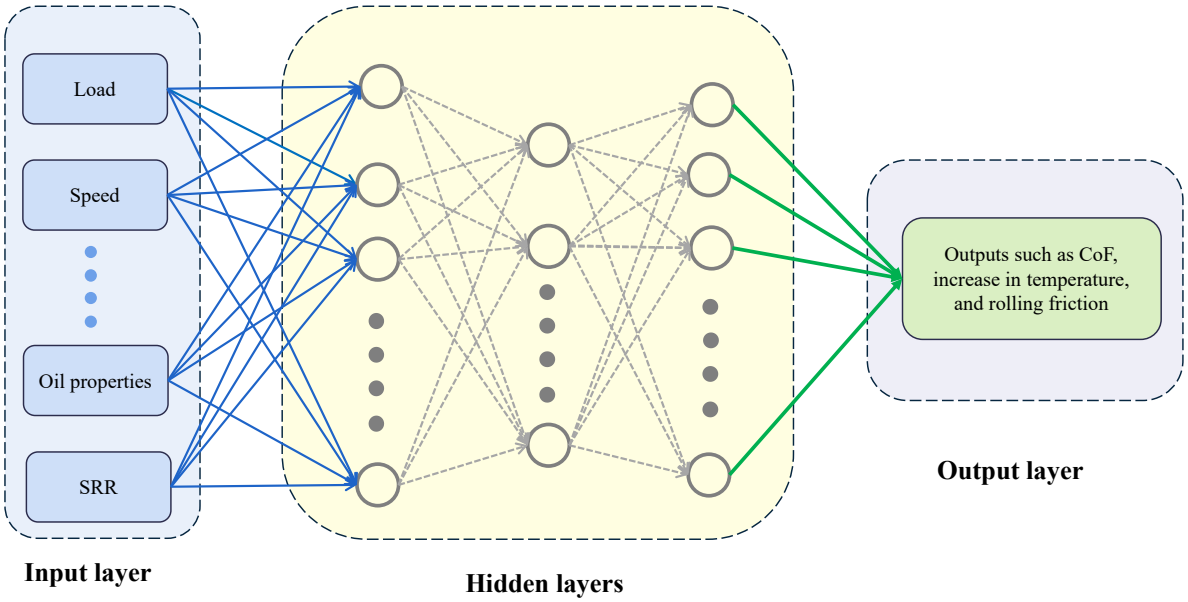

Figure 2. A schematic of ANN

stability, the Aitken relaxation method [33] has been applied to the pressure and temperature equations, as well as mutual approach calculations.

Validation of the numerical solver for TEHL contact is conducted and presented in the appendix for the sake of brevity.

2.3. Machine learning architecture

To predict tribological parameters such as mutual approach (H_0), minimum film thickness ($H_{\min}$), central film thickness at contact (H_c), coefficient of friction (CoF), maximum temperature ($T_{\max}$), and rolling friction force (F_R), we employed ANN models with a feedforward architecture. Note that the film thickness metrics are expressed in non-dimensional form, while temperature rise is reported in degrees Celsius. Additionally, friction-related outputs (CoF and F_R) are inherently normalised by the applied load.

Each model comprised twelve input features representing operating conditions and material properties, followed by a variable number of hidden layers and neurons, and a single-output layer producing the target prediction. A schematic representation of the network is shown in Figure 2. The architecture and hyperparameters were optimised using Optuna [34] with the objective of minimising validation loss and improving generalisation on unseen data. The optimisation process explored a wide search space, including the number of hidden layers (ranging from two to six), neurons per layer (32–512 on a logarithmic scale), learning rate (10^{-5} to 3×10^{-3}), dropout rate (0.01–0.25), and weight decay (10^{-6} to 10^{-3}). This systematic tuning ensured that each model was tailored to the complexity of its respective output.

The optimisation phase consisted of 200 trials per model, with each trial running up to 500 iterations. To reduce computational cost, early stopping was implemented using the MedianPruner strategy, which terminated trials after 200 iterations if no improvement in validation loss was observed. Once the best-performing configuration was identified, final training was conducted using the optimal parameters for a maximum of 50,000 iterations. Within each network, a hyperbolic tangent activation function was applied between layers to introduce non-linearity, and dropout layers were incorporated to mitigate overfitting. An adaptive learning rate strategy was employed, halving the learning rate whenever validation loss plateaued for 500 iterations, down to a minimum of 10^{-6}. Training was terminated if the validation loss did not improve by at least 10^{-6} over 2,000 iterations.

This systematic optimisation process improved the generalisation capability of the models, enabling accurate prediction of complex TEHL outputs. Nevertheless, the accuracy of certain outputs,

Table 1. Ranges of input variables and constant parameters

Variable	Range / Value	Unit
U_{ave}	1–6	m/s
F	50–800	kN/m
R_{eq}	5–15	mm
SRR	0–1.5	–
μ_R	0.01–0.3	Pa s
α_p	10–25	1/GPa
β	0.02–0.05	1/K
τ_0	2–10	MPa
k_{oil}	0.1–0.3	W/(m K)
$C_{p,\text{oil}}$	1500–2800	J/(kg K)
$C_{p,s}$	300–600	J/(kg K)
k_s	10–60	W/(m K)
Constant parameters		
E	200	GPa
T_0	313.15	K
ν	0.3	–
ρ_s	7850	kg/m^3
$\rho_{l,R}$	800	kg/m^3

such as traction curves, remained sensitive to network configuration, a topic discussed further in Section 3.3.

2.3.1. Dataset

The classical Reynolds equations were solved to generate a comprehensive dataset for training the ANN model, capturing a wide range of operating conditions and material properties relevant to TEHL contact modelling. After filtering out non-converged cases, approximately 36,000 samples were retained for training. The input ranges and constants used throughout the study are summarised in Table 1. The oil property ranges were established based on literature data, and the dataset spans low to high speeds and loads.

A few practical notes on the dataset:

- Samples were generated using the Latin Hypercube Sampling (LHS) method, resulting in a well-distributed input space. The distributions of input variables are shown in Figure 3.
- The SRR range was set between 0 and 1.5 to ensure validity of the Carslaw-Jaeger condition.
- To improve the accuracy of CoF prediction in the low SRR region, where frictional behaviour is highly sensitive, 500 cases were generated with a fixed SRR of 0 (pure rolling condition).
- The inlet temperature was held constant. Since temperature and oil properties are strongly correlated, oil properties were treated as inputs calculated at a given temperature. This approach enables the model to predict temperature rise and generalises its applicability to different oils and operating temperatures.

In addition to input distributions, the distribution of output variables plays a critical role in effective model training. Figure 4 presents histograms for four representative outputs: minimum film thickness, rolling friction, maximum temperature, and CoF. The minimum film thickness data is highly concentrated in the lower range ($H_{\text{min}} < 1$), while thicker films ($H_{\text{min}} > 2$) occur rarely and are typically associated with low loads, high speeds, and high-viscosity oils. Both CoF and rolling friction exhibit skewed distributions, with most samples clustered within $0.005 < \text{CoF} < 0.025$ and $0.0002 < F_R < 0.004$. This sparsity at the extremes may hinder generalisation across the full output space, although it reflects the inherent non-linear relationships between inputs and outputs. In contrast, the distribution of maximum temperature is relatively uniform, particularly for values below 410 K,

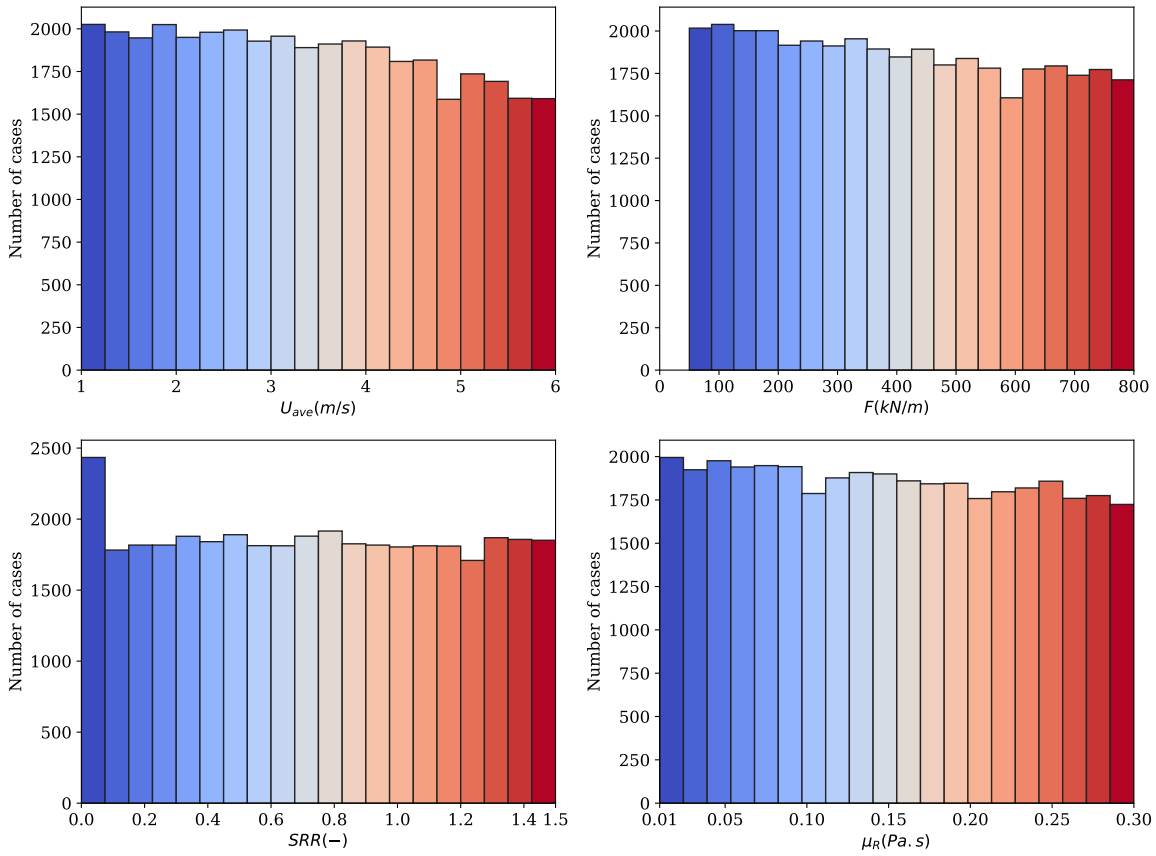

Figure 3. Histogram of selected input variables before removing outliers: (a) average velocity, (b) applied load, (c) SRR, and (d) ambient viscosity.

which helps mitigate bias toward specific regions and enhances the learning performance of the ANN models.

2.3.2. Outlier Detection

Initial filtering was performed based on physical constraints to ensure the validity of the dataset. Cases exhibiting extremely low film thickness indicative of mixed-EHL conditions, and violating the minimum Peclet number threshold ($Pe < 5$) were excluded. This physical filtering accounted for about 3 % of the total dataset but was essential to maintain consistency with the TEHL regime.

Beyond physical checks, statistical outlier detection was applied to identify samples exhibiting irregular patterns in the output parameters, such as the CoF and temperature rise. Such outliers, if retained, could bias the training process and degrade the generalisation performance of the neural network.

In this study, a combination of Isolation Forest (IF) and Local Outlier Factor (LOF) algorithms are employed to leverage their complementary strengths. The IF method isolates observations by recursively partitioning the feature space, effectively identifying *global outliers* that deviate strongly from the overall distribution [35]. The LOF method compares local densities with nearest neighbours, detecting *local outliers* that may be consistent globally but atypical in their immediate neighbourhood [36].

Three experiments were conducted to evaluate the impact of outlier removal on CoF and temperature rise models. Initially, only the common outliers identified by both methods were removed, leading to marginal improvements in parity plots and statistical metrics. Subsequently, outliers detected individually by each method were removed, with each method set to flag approximately 3 % of samples. This approach consistently improved the coefficient of determination (R^2) across training, validation, and test sets, although gains remained modest (below 1 %) due to the already high baseline accuracy

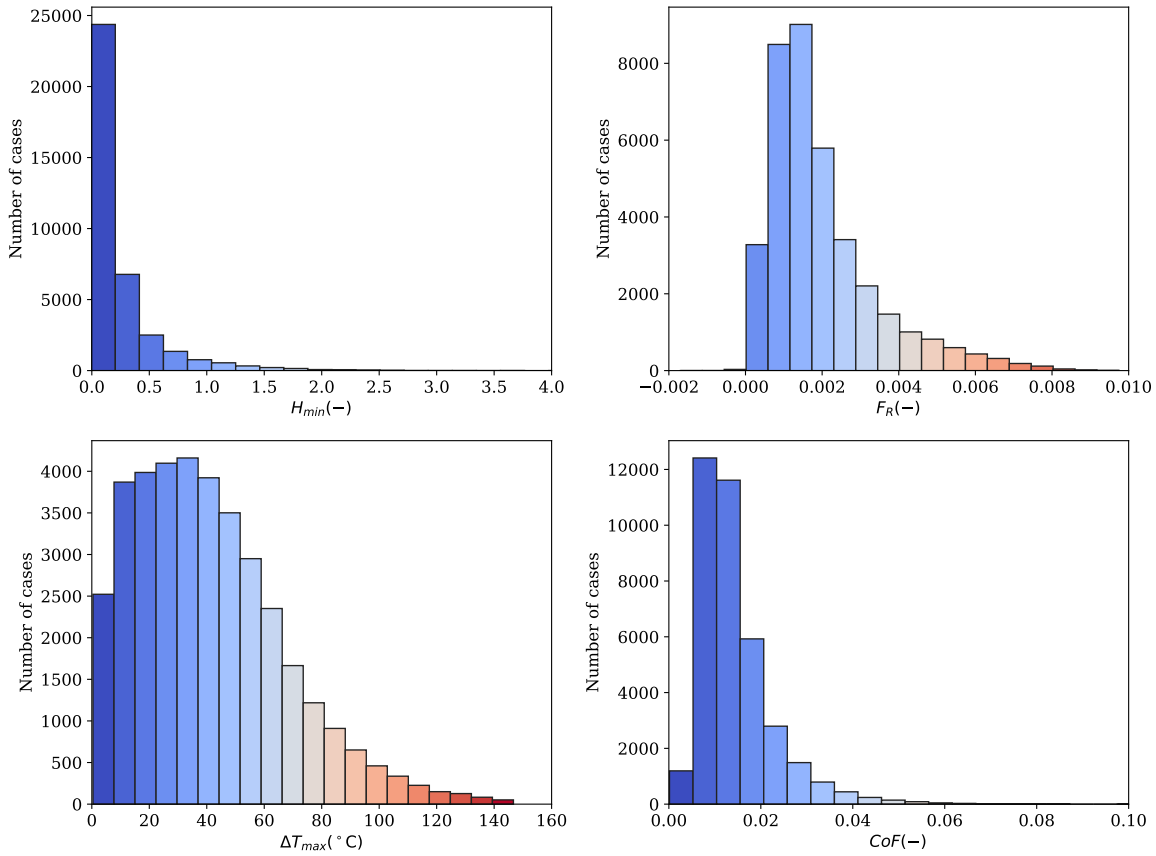

Figure 4. Overall distribution of output variables prior to outlier removal: (a) minimum film thickness, (b) rolling friction, (c) maximum temperature, and (d) CoF.

(R^2 in the range of 98 % to 99 %). Scatter in the parity plots became noticeably tighter, indicating enhanced robustness, with LOF-based removal showing the strongest effect.

Finally, we removed 1 % of global outliers using IF and 2 % of local outliers using LOF, assigning higher weight to LOF due to its superior performance. Importantly, outlier removal was performed separately for each output variable. Each model excluded all detected outliers for its target, regardless of whether these samples were also outliers for other outputs. While some outliers overlapped across outputs, each variable retained its own set of removed samples rather than only common cases. This separate treatment is preferred because each output may have distinct statistical outliers. Removing only the intersection of outliers across variables would leave target-specific irregular samples in the training set. By filtering per output, we ensure that each model is trained on data that is clean and representative for its specific output target, while maintaining the coverage of the input space.

While overall output distributions were shown before in Figure 4, Figure 5 highlights the detected outliers in the maximum temperature rise and CoF after applying physical filtering. In these plots, red markers indicate samples identified as outliers by the IF method, while orange markers correspond to those flagged by the LOF method. It is evident that the IF method predominantly flags points exhibiting significant deviation or unusually high variance compared to the global data trend, corresponding to global outliers. Conversely, the LOF method identifies samples that appear globally consistent yet deviate from their immediate neighbourhood in feature space, revealing locally inconsistent data patterns. This complementary detection behaviour confirms that the two methods capture distinct classes of abnormal cases.

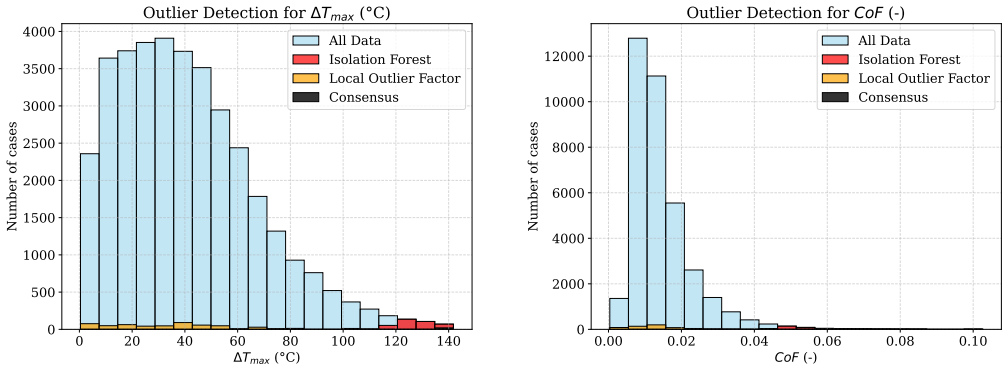

(**a**) (**b**)

Figure 5. Outlier detection results for maximum temperature and CoF after physical filtering.

Table 2. Performance metrics by output and set type.

	R^2			RMSE			MAPE (%)		
Output	Train	Val	Test	Train	Val	Test	Train	Val	Test
H_0	0.999712	0.999666	0.999355	0.005739	0.006180	0.008165	0.008812	0.012251	0.014464
H_{min}	0.999719	0.998828	0.999100	0.004195	0.008578	0.007518	0.025707	0.027937	0.028280
H_c	0.999590	0.999076	0.999009	0.005789	0.008609	0.009127	0.026909	0.029492	0.029024
CoF	0.997265	0.989347	0.985720	0.000382	0.000761	0.000861	0.022033	0.029322	0.031211
T_{max}	0.998536	0.996305	0.996185	0.948709	1.482330	1.523459	0.023484	0.029949	0.029521
F_R	0.997638	0.995179	0.995547	0.000066	0.000096	0.000093	0.040911	0.045940	0.040249

3. Results

This section presents a detailed discussion on the prediction accuracy of the ANN model and the relative importance of each input feature. It also includes several evaluation examples used to assess the model's performance in predicting TEHL outputs across a range of operating conditions and oil properties.

3.1. Model Performance and Error Analysis

Following hyperparameter optimisation, the final training was conducted using the 12 input features listed in Table 1. The performance of the developed ANN models for predicting key tribological outputs—namely minimum and central film thicknesses (H_{min}, H_c), coefficient of friction (CoF), maximum temperature rise ($\Delta T_{\max}$), and rolling friction force (F_R)—is summarized in Table 2. Evaluation metrics include the coefficient of determination (R^2), root mean squared error (RMSE), and mean absolute percentage error (MAPE), defined as:

$$R^2 = 1 - \frac{\sum_{i=1}^{n}(y_i - \hat{y}i)^2}{\sum_{i=1}^{n}(y_i - \bar{y})^2}, \quad \text{RMSE} = \sqrt{\frac{1}{n}\sum_{i=1}^{n}(y_i - \hat{y}i)^2}, \quad \text{MAPE} = \frac{1}{n}\sum_{i=1}^{n}\left|\frac{y_i - \hat{y}i}{y_i}\right|. \tag{17}$$

The ANN models for film thicknesses exhibit exceptional accuracy ($R^2 \geq 0.999$) with minimal RMSE and MAPE values, consistent with previous machine-learning studies on film thickness prediction [20]. The model for $\Delta T_{\max}$ also performs strongly ($R^2 = 0.9914$), with low RMSE and MAPE across training, validation, and test sets, aligning with the previous study for maximum temperature prediction [19].

The model for F_R yields high accuracy ($R^2 = 0.9955$ in the test set), with low RMSE and MAPE, indicating strong generalisation. Notably, F_R is the rolling friction normalised by the applied load (refer to Equation (15)), such that $F_R = \frac{F_{roll}}{F} = \frac{e_p}{R_{eq}}$, where e_p is the pressure distribution eccentricity.

The CoF model performs adequately, though with relatively lower accuracy ($R^2 = 0.9857$ and MAPE $= 0.031\,\%$). Prediction errors are more pronounced at higher friction values (CoF > 0.03),

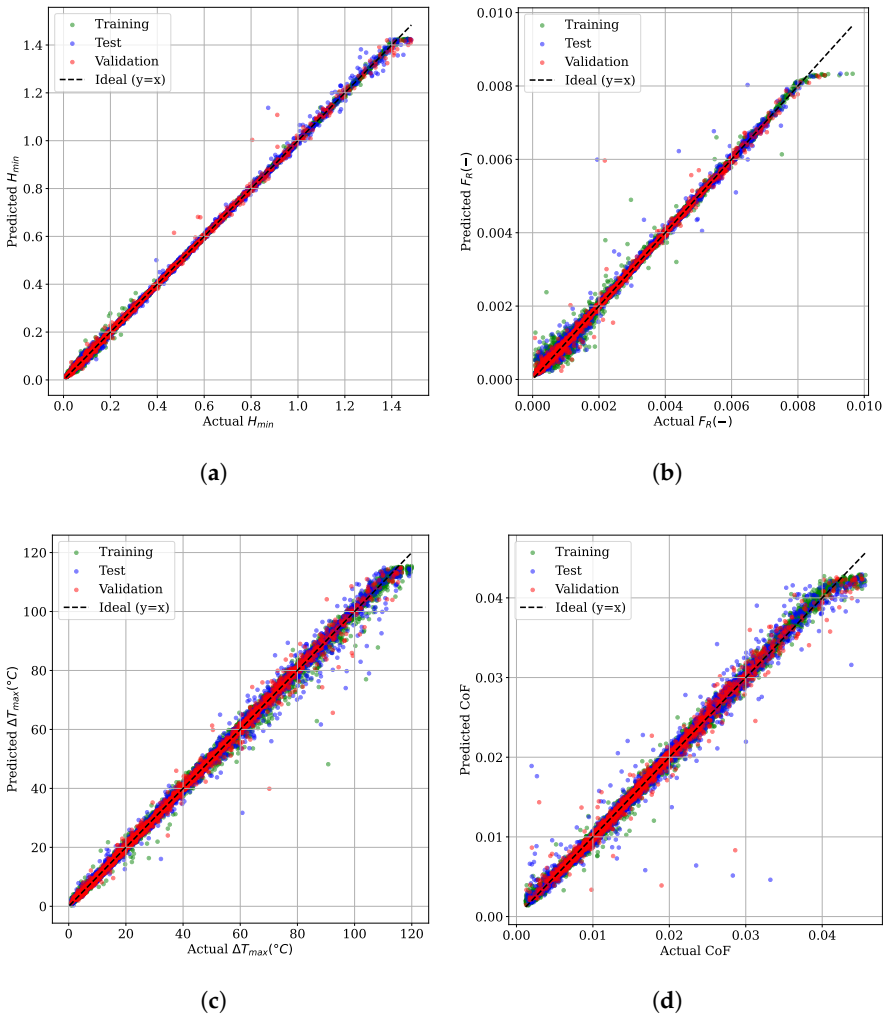

Figure 6. Prediction accuracy of ANN models: (**a**) minimum film thickness, (**b**) rolling friction force, (**c**) maximum temperature, and (**d**) coefficient of friction.

suggesting the model could benefit from additional training data in these regimes. This issue will be discussed in detail in subsequent sections. Moreover, without removing the outliers for the CoF model, the coefficient of determination was lower ($R^2 = 0.965$), and the parity plot showed more scatter.

Figure 6 presents parity plots for selected outputs across the training, validation, and test sets. Film thickness predictions exhibit high fidelity, with minor deviations observed under low-load, high-speed conditions that result in very thick films. For the CoF, moderate scatter is evident, particularly at higher friction values, though the overall predictive performance remains acceptable given the inherent complexity of frictional behaviour.

The parity plot for rolling friction (F_R) shows generally good clustering along the 1:1 reference line, with slight dispersion at the extremes—specifically for very low values ($F_R < 0.001$) and very high values ($F_R > 0.008$). Predictions for the maximum temperature rise ($\Delta T_{\max}$) align closely with the true values across all datasets, with tight clustering and only a few scattered data points.

Overall, the consistently high R^2 values and low error metrics across most outputs confirm the robustness and generalisation capability of the developed ANN models.

3.2. Features importance

The feature importance analysis for the ANN models is presented in Figure 7, based on the SHAP (SHapley Additive exPlanations) framework [37]. Using SHAP, we can quantify the contribution of each input variable to the model prediction relative to a baseline output, defined as the mean model

response over 200 background samples. Each feature receives an additive contribution such that the sum of all SHAP values equals the model output. Hence, SHAP values indicate how each feature shifts the prediction away from the baseline, thereby reflecting the model's sensitivity to that feature.

To ensure physically meaningful attribution, the analysis was conducted using dimensional film thickness metrics (H_{min}, H_c, and H_0). Non-dimensional forms are normalised by load and equivalent radius—both of which are also input features—introducing interdependencies that can distort attribution. Using dimensional quantities avoids this coupling and provides clearer insight into the physical influence of each input.

Figure 7 illustrates the percentage contributions (SHAP value divided by the baseline and multiplied by 100) for each output, enabling rapid visual assessment of input parameter impact. The dominant features vary across the predicted quantities, and the key observations are summarised below:

- **Central film thickness (H_c):** The analysis identifies average speed (U_{ave}), ambient viscosity (μ_R), and the piezo-viscous coefficient (α_p) as the three most dominant factors governing H_c. Other influences arise from the applied load (F), equivalent radius (R_{eq}), and SRR. Physically, the conditions in the inlet zone—primarily determined by U_{ave}, μ_R, and α_p—control lubricant entrainment and thus establish the central film thickness. The SRR affects H_c indirectly via thermal effects: increased sliding generates more heat, reducing lubricant viscosity in the inlet and contact region, thereby decreasing film thickness. In contrast, the thermal properties of the lubricant (k_{oil}, $C_{p,oil}$) and solids (k_s, $C_{p,s}$), as well as the Eyring stress (τ_0), show negligible influence within the studied range. This suggests that approximate engineering values for these thermal properties are sufficient for H_c estimation.
- **Minimum film thickness (H_{min}):** Similar to H_c, H_{min} is primarily governed by U_{ave} and μ_R. However, SRR exhibits greater relative importance for H_{min}, ranking as the second most influential feature. This aligns with the fact that H_{min} is affected by both inlet flow conditions and local phenomena within the contact zone [38]. Since it typically occurs near the contact exit, H_{min} is particularly sensitive to shear and thermal effects—both of which are strongly influenced by SRR.
- **Mutual approach (H_0):** The mutual approach, representing the elastic deformation of the contacting bodies, is dominated by the applied load (F), with only minor contributions from μ_R and U_{ave}. This reflects the primarily elastic nature of deformation, which scales almost linearly with load. Consequently, the overall stiffness of the TEHL contact—considering both solid and lubricant compliance—is mainly dictated by the solid deformation response.
- **Rolling friction (F_R):** The rolling friction is mainly influenced by F, μ_R, and U_{ave} followed by α_p and SRR. Rolling friction originates from the asymmetry of the TEHL pressure distribution relative to the contact centre. At high loads, the pressure profile becomes nearly symmetric (Hertzian-like), reducing eccentricity and thus rolling friction. Conversely, higher speeds or viscosity increase lubricant entrainment and extend the pressure tail toward the inlet, enhancing asymmetry and consequently F_R.
- **Maximum temperature rise ($\Delta T_{\mathbf{max}}$):** The maximum temperature rise is predominantly governed by SRR, as it directly controls viscous heat generation, which is the most dominant mechanism in TEHL contacts [39]. The piezo-viscous coefficient (α_p) and temperature-viscosity coefficient (β) also play significant roles: larger α_p or smaller β amplify heat generation due to enhanced pressure-viscosity sensitivity and reduced thermal thinning, respectively. The average speed (U_{ave}) ranks fourth, influencing both shear rate and convective heat dissipation. Additionally, higher loads (F) cause moderate film thinning, intensifying shear heating and contributing to larger $\Delta T_{\max}$.
- **Coefficient of friction (CoF):** The CoF is most sensitive to α_p and SRR. The piezo-viscous coefficient governs the high-pressure viscosity behaviour and, therefore, the shear stress. Increasing α_p results in thicker films and higher friction. SRR is the second most influential parameter, reflecting the typical traction curve trend: CoF increases with SRR in the linear regime, then decreases due

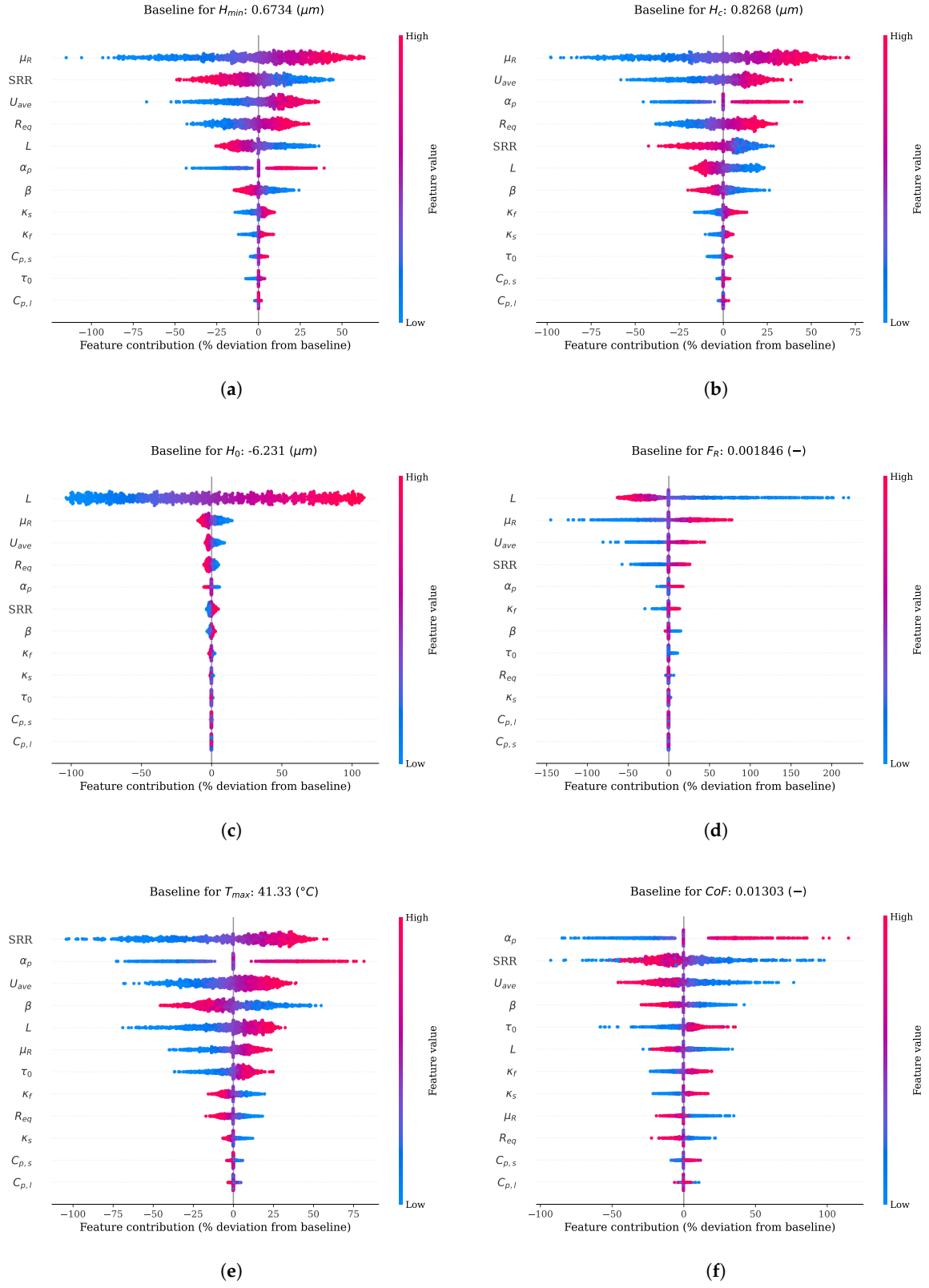

Figure 7. Relative input contributions to the prediction of each TEHL contact output. The baseline value and the percentage contribution (SHAP value divided by the baseline and multiplied by 100) are shown for each output: (a) minimum film thickness, (b) central film thickness, (c) mutual approach, (d) rolling friction, (e) maximum temperature increase, and (f) coefficient of friction.

to shear thinning and thermal softening. Average speed (U_{ave}) ranks third; while higher speed thickens the film, it also increases shear rate, leading to a net rise in CoF. The temperature-viscosity coefficient (β) also affects CoF by determining thermal stability of viscosity—a lower β implies a more thermally stable lubricant, yielding higher friction. The Eyring stress (τ_0) and thermal conductivities (k_{oil}, k_s) further influence CoF by modifying the shear and temperature fields within the contact.

3.3. Evaluation examples

The predictive capability of the trained models was assessed using unseen TEHL cases. Four representative scenarios were selected, each with distinct operating conditions and material properties, as summarised in Table 3. For these cases, the SRR was varied from 0 to 1.5 to generate traction curves. Predictions for key outputs—CoF, rolling friction, maximum temperature, and minimum film thickness—were compared against reference solutions obtained from Reynolds-based simulations (Figure 8).

To ensure meaningful error evaluation for the CoF model, data points at SRR $= 0$ were excluded because true friction values are near zero, which would otherwise lead to disproportionately large relative errors and misrepresent overall accuracy.

Table 3. Inputs for evaluation examples

Variable	Unit	Case 1	Case 2	Case 3
μ_R	Pa s	0.02	0.1	0.18
U_{ave}	m/s	3.5	2.5	1.5
F	kN/m	200	400	500
R_{eq}	mm	10	7.5	12
α_p	1/GPa	18.1	21	15
β	1/K	0.038	0.03	0.045
τ_0	MPa	5.5	4.5	7
k_{oil}	W/(m K)	0.2	0.17	0.14
$C_{p,\text{oil}}$	J/(kg K)	2200	2300	2000
$C_{p,s}$	J/(kg K)	450	450	420
k_s	W/(m K)	47	47	25

The results show excellent agreement between ANN prediction and reference solutions in both trend and magnitude. The CoF model accurately captures the nonlinear traction behaviour, aided by targeted data enrichment in low-SRR regions (Section 2.3.1). Among all outputs, the largest deviations occur in rolling friction for Case 1; however, the model still follows the correct trend and maintains acceptable accuracy (about 4.8 %).

For Case 1, the maximum relative errors are 2.98 % for minimum film thickness, 4.80 % for rolling friction, and less than 14.52 % for maximum temperature prediction. Although this percentage appears high for temperature, the absolute deviation in maximum temperature rise is only 0.68 °C, which remains within acceptable engineering margins. CoF predictions show higher local errors near SRR $= 0$, yet the overall trend aligns well with the reference curve, yielding a mean error of 2.73 %.

Case 2 demonstrates similar accuracy, while Case 3 shows slightly higher deviations—up to 3.22 % for film thickness and 4.3 % for rolling friction—yet CoF remains robust (mean error 3.83 %).

In addition to predictive accuracy, computational efficiency is a critical consideration for practical deployment. The Reynolds-based TEHL solver, implemented in Python, typically requires between 1 and 5 minutes per simulation, depending on operating conditions. In contrast, the ANN model, implemented using the PyTorch framework [40], achieves substantial acceleration. For a batch of one million evaluations, the model requires approximately 1 second on CPU and 0.4 seconds on GPU. This reduction in computational cost—by several orders of magnitude—enables real-time integration into system-level simulations and supports rapid design iterations for tribological components.

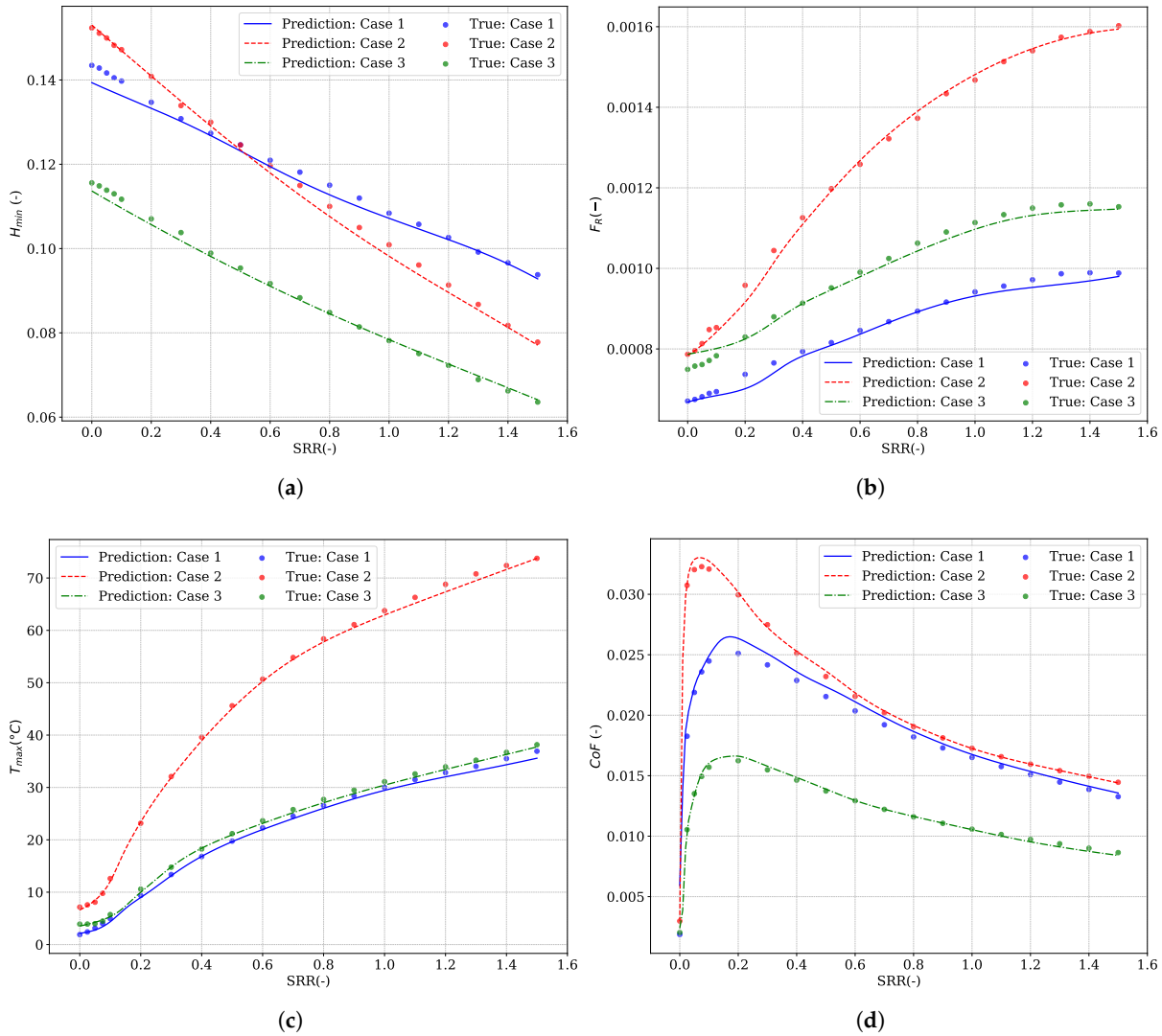

Figure 8. Comparison of ANN predictions and Reynolds solution for three distinct examples. (**a**) minimum film thickness, (**b**) rolling friction force, (**c**) maximum temperature, and (**d**) coefficient of friction.

Reynolds-based simulations for these cases require tight convergence tolerances and numerous iterations to suppress numerical noise, particularly under high-viscosity and high-speed conditions. In contrast, the ANN models deliver sufficiently accurate predictions without manual tuning, leveraging high-dimensional interpolation across the dataset. This highlights a key advantage of ML over traditional solvers.

An analysis of Figure 8 reveals that the ANN model exhibits reduced prediction accuracy for the CoF, particularly in the low SRR region. This topic will be discussed in detail in the following section.

3.4. Improvement strategies for CoF prediction

An assessment of Figure 8 and Figure 6 reveals that the performance of the CoF model deteriorates in specific regions, particularly at very low and very high CoF values. Note that very sparse CoF data has already been detected as an outlier and removed from the dataset before training. In this section, we analyse the root causes of this behaviour and discuss various strategies implemented to enhance the predictive accuracy of the CoF model in these regions. Among the tested approaches, only adaptive sampling proved effective.

The largest prediction errors occur at low CoF and low SRR conditions. Several preprocessing and feature-engineering techniques were evaluated to mitigate this issue, including logarithmic transformations of the SRR input (e.g., $\ln(1 + \mathrm{SRR})$), the introduction of dimensionless variables such

Algorithm 2 Adaptive sampling for TEHL parameter exploration

Require: Existing input parameters $\mathbf{X}$, corresponding CoF values $\mathbf{y}$, number of new samples per iteration n, number of iterations n_{iter}, trained ANN model f_{ANN}
Ensure: New parameter samples $\mathbf{X}_{\text{new}}$ targeting low-density CoF regions

```
Load existing dataset (X, y) and trained model f_ANN
for k = 1 to n_iter do
    Compute histogram of y with n_b bins to identify low-density regions
    Assign sampling weights to bins inversely proportional to their densities
    Generate candidate inputs X_cand via Latin Hypercube Sampling
    Predict CoF values: ŷ_cand ← f_ANN(X_cand)
    Select n samples from X_cand falling into low-density CoF bins
    for each candidate x_i ∈ X_cand do
        Run preliminary TEHL simulation (e.g., 300 iterations) to estimate CoF (ŷ_i)
        if ŷ_i falls within a low-density bin then
            Add x_i to X_new
            Run full TEHL simulation for x_i to compute accurate CoF
        end if
    end for
    Update dataset: X ← X ∪ X_new; update y accordingly
end for
return X_new
```

as the Peclet number, and logarithmic or quantile transformations of the CoF output. None of these yielded a measurable improvement in accuracy.

Further attempts involved extending the input space with polynomial terms (e.g., SRR^2), which marginally increased R^2 but did not resolve the low-SRR discrepancies. Other transformation methods addressing data skewness, such as power transformations [41], also showed no benefit. Likewise, synthetic data augmentation to enrich the low-SRR domain failed to significantly reduce prediction errors.

Collectively, these findings indicate that conventional feature engineering and data transformation methods are insufficient to resolve the model's limitations in sparse regions of the output space. Improving generalisation requires either advanced modelling techniques or the inclusion of additional high-fidelity data specifically targeted at under-represented regions.

3.4.1. Adaptive sampling

To improve the data distribution in sparse regions of the CoF space—particularly at very low and high CoF values—an adaptive sampling strategy was implemented. This approach utilises a pre-trained ANN model as a surrogate to guide the generation of new input parameters that specifically target underrepresented regions in the output space.

A summary of this algorithm is provided in Algorithm 2. At each iteration, the existing dataset is analysed to identify gaps in the CoF distribution. The CoF values are first filtered to remove invalid entries and then binned into a fixed number of intervals to construct a histogram. This histogram is used to detect low-density regions, and sampling weights are assigned inversely proportional to the bin densities. Regions with fewer data points are thereby prioritised in the sampling process.

An extensive set of candidate input vectors is generated using LHS, ensuring uniform coverage of the input space. The ANN model is then used to predict the CoF values corresponding to these candidates. Samples predicted to lie in low-density CoF intervals are selected for further evaluation.

To reduce computational cost, a coarse TEHL simulation (limited to a small number of solver iterations) is performed for each selected candidate to compute a preliminary CoF estimate. Candidates whose preliminary CoF remains within low-density regions are retained, and a full-resolution TEHL simulation is conducted to obtain accurate outputs. These new samples are then added to the training dataset, and the histogram is updated before the next iteration.

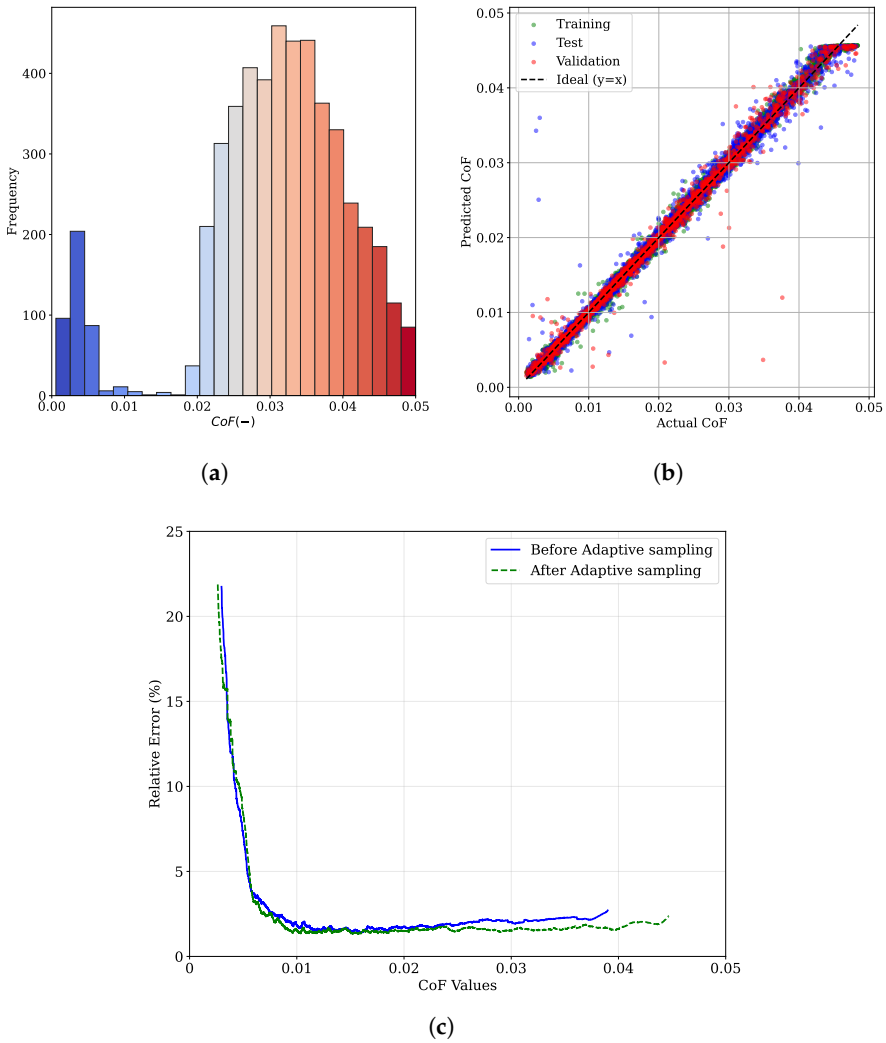

Figure 9. (a) Distribution of additional CoF samples generated through adaptive sampling, (b) parity plot showing improved prediction accuracy after incorporating these samples, and (c) comparison of moving average prediction error across different CoF ranges before and after adaptive sampling.

This adaptive sampling framework enables targeted augmentation of the dataset in critical regions of the CoF space, enhancing model generalisation while minimising the number of expensive TEHL simulations. It also allows the surrogate ANN model to iteratively improve by focusing learning on regions where prediction uncertainty or data scarcity is highest.

After applying the adaptive sampling strategy and removing identified outliers, a total of 4900 new data points were added to the original dataset (see Section 2.3.1). The histogram in Figure 9-a shows the CoF distribution of the newly generated data. As intended, the added samples are concentrated in the previously underrepresented regions, particularly below 0.005 and above 0.022. At the same time, the densely populated area of the original dataset ($0.005 < \text{CoF} < 0.022$) contains relatively few new samples. This targeted augmentation effectively addresses the data imbalance and enhances the overall coverage of the CoF domain.

Following dataset augmentation, the ANN model was retrained (with optimisation of the hyperparameters and an outlier detection) for CoF prediction. As illustrated in Figure 9-b, the updated parity plot demonstrates reduced scatter and improved agreement, particularly in the higher CoF region where previous predictions exhibited notable errors. The coefficient of determination (R^2) on the test and validation sets improved to approximately 99.1 %, indicating a substantial enhancement in model performance.

Figure 9-c illustrates the moving average of relative prediction error across different CoF ranges before and after adaptive sampling. This representation highlights where improvements are most pronounced. The largest reduction occurs at very low CoF values (< 0.005), where the original model exhibited high relative errors due to sparse training data. Although relative error appears large in this region, it is primarily a scaling effect because the absolute CoF values are extremely small, meaning the absolute error remains negligible. Moderate improvements are also observed for CoF values above 0.025, where adaptive sampling enriched previously underrepresented high-friction cases.

Overall, the final model benefits from a relatively more uniformly distributed training set, enabling more accurate and reliable predictions across the full range of CoF values.

4. Conclusions

This study presented a data-driven modelling framework for TEHL line contacts, leveraging ANN architectures trained on simulation data that incorporate non-Newtonian rheology and thermal effects, which are often overlooked in previous studies, particularly in friction prediction. In this study, ANN models were developed and validated for predicting key tribological outputs in TEHL line contacts, including film thickness metrics, CoF, rolling friction, and maximum temperature rise. The main contributions and findings are as follows:

1. The ANN models achieved near-perfect accuracy for film thickness parameters (H_0, $H_{\min}$, and H_c), rolling friction (F_R), and maximum temperature ($T_{\max}$), with R^2 values exceeding 0.995 across training, validation, and test sets. These results confirm that data-driven models can replicate the complex multi-physics behaviour of TEHL contacts without explicit numerical solvers.
2. Initial CoF predictions exhibited relatively reduced accuracy in sparse regions of the output space, particularly at very low and high friction values. By implementing an adaptive sampling strategy that targeted underrepresented regions, the dataset was enriched with 4,900 additional samples. This approach improved the CoF model's R^2 to approximately 0.991 and reduced scatter in parity plots, demonstrating the effectiveness of targeted data augmentation.
3. Sensitivity analysis revealed that operating conditions such as average speed (U_{ave}), SRR, ambient viscosity (μ_R), and piezo-viscous coefficient (α_p) exert the strongest influence on most of the outputs. Thermal properties of the lubricant and solids showed secondary importance, suggesting that approximate engineering values for these parameters are sufficient for accurate predictions within the studied range.
4. The ANN models were validated against unseen TEHL cases, including traction curves across varying SRR values. Predictions closely matched reference solutions, with mean errors below 5 percent for most outputs. These results confirm the robustness and generalisation capability of the proposed framework.
5. Compared to conventional Reynolds-based TEHL solvers, which require minutes per simulation under strict convergence criteria, the ANN models deliver predictions in microseconds when running a batch of them on both CPU and GPU. This reduction in computational cost enables real-time integration into system-level simulations of gears, bearings, and other machine elements, supporting rapid design iterations and power-loss estimation.

Future work will focus on extending the methodology toward full-field prediction of TEHL quantities (e.g., two-dimensional temperature), as well as transient operating conditions. In addition, incorporating uncertainty quantification will enable reliability assessment and confidence estimation in model predictions.

Author Contributions: P.H. was responsible for the conceptualization, software, methodology development, formal analysis and investigation, visualization, and writing of the original draft. D.F. contributed to writing, review, and editing of the manuscript, and funding acquisition, resources, and provided supervision.

Funding: This work was supported by the **ROLUX project**, funded by Flanders Make, and the **CORE project**, funded by VLAIO. The authors gratefully acknowledge this support.

Data Availability Statement: Data sets generated during the current study are available from the corresponding author on reasonable request.

Conflicts of Interest: The authors declare no conflicts of interest.

Abbreviation

ANN Artificial Neural Network

CoF Coefficient of Friction

EHL Elastohydrodynamic Lubrication

FFT Fast Fourier Transform

FVM Finite Volume Method

GPR Gaussian Process Regression

IF Isolation Forest

LHS Latin Hypercube Sampling

LOF Local Outlier Factor

ML Machine Learning

PDE Partial Differential Equation

SRR Slide-to-Roll Ratio

TEHL Thermo-Elastohydrodynamic Lubrication

Nomenclature

Greek letters

α	Piezo-viscous coefficient	$[1/\mathrm{Pa}]$
β	Temperature-viscosity coefficient	$[1/\mathrm{K}]$
β_T	Thermal expansion coefficient	$[1/\mathrm{K}]$
$\dot{\gamma}$	Shear rate	$[1/\mathrm{s}]$
η	Non-Newtonian viscosity	$[\mathrm{Pa\,s}]$
μ	Newtonian viscosity	$[\mathrm{Pa\,s}]$
ρ	Density	$[\mathrm{kg/m^3}]$
τ	Shear stress	[Pa]
τ_0	Eyring stress	[Pa]
θ	Liquid volume fraction	[-]
ϑ	Poisson's ratio	[-]

Latin letters

$\overline{D}$	Dimensionless deformation	$[-]$
A	Surface area	$[\mathrm{m^2}]$
a_H	Hertzian half contact width	[m]
C_p	Heat capacity	$[\mathrm{J/(kg\,K)}]$

E	Elastic modulus	[Pa]
e_p	Pressure eccentricity	[m]
F	External load applied on the contact	[N]
H	Dimensionless film thickness	[−]
h	Film thickness	[m]
k	Thermal conductivity	[W/(m K)]
P	Dimensionless pressure	[−]
p	Pressure	[Pa]
q	Heat flux	[W/m^2]
R	Equivalent radius of curvature	[m]
T	Temperature	[K or °C]
u	Velocity	[m/s]

Subscripts and superscripts

eq	Equivalent
f	Fluid
H	Hertzian
R	Reference condition
s	Sliding or solid material
w	Wall

References

1. Havaej, P.; Degroote, J.; Fauconnier, D. A quantitative analysis of double-sided surface waviness on TEHL line contacts. *Tribology International* **2023**, *183*, 108389. https://doi.org/https://doi.org/10.1016/j.triboint.2023.108389.
2. Habchi, W. A Full-system finite element approach to elastohydrodynamic lubrication problems. PhD thesis, L'Institut National des Sciences Appliquées de Lyon, 2008.
3. Ai, A.; Cheng, H. Numerical Simulation of Elastohydrodynamically Lubricated Contacts With Rough Surfaces. *Applied Mechanics Reviews* **1993**, *47*, S221–S227. https://doi.org/10.1115/1.3124411.
4. Venner, C.H.; Lubrecht, A.A. Multigrid techniques: A fast and efficient method for the numerical simulation of elastohydrodynamically lubricated point contact problems. *Proceedings of the Institution of Mechanical Engineers, Part J: Journal of Engineering Tribology* **2000**, *214*, 43–62, [https://doi.org/10.1243/1350650001543007]. https://doi.org/10.1243/1350650001543007.
5. Venner, C.H.; Wijnant, Y.H. Validation of EHL Contact Predictions under Time Varying Load. *Proceedings of the Institution of Mechanical Engineers, Part J: Journal of Engineering Tribology* **2005**, *219*, 249–261, [https://doi.org/10.1243/135065005X33865]. https://doi.org/10.1243/135065005X33865.
6. Liu, Y.; Wang, Q.J.; Zhu, D.; Wang, W.; Hu, Y. Effects of Differential Scheme and Viscosity Model on Rough-Surface Point-Contact Isothermal EHL. *Journal of Tribology* **2009**, *131*. https://doi.org/10.1115/1.2842245.
7. Habchi, W.; Issa, J.S. An Exact and General Model Order Reduction Technique for the Finite Element Solution of Elastohydrodynamic Lubrication Problems. *Journal of Tribology* **2017**, *139*, 051501, [https://asmedigitalcollection.asme.org/tribology/article-pdf/139/5/051501/6290851/trib_139_05_051501.pdf]. https://doi.org/10.1115/1.4035154.

8. Scurria, L.; Fauconnier, D.; Jiránek, P.; Tamarozzi, T. A Galerkin/hyper-reduction technique to reduce steady-state elastohydrodynamic line contact problems. *Computer Methods in Applied Mechanics and Engineering* **2021**, *386*, 114132. https://doi.org/https://doi.org/10.1016/j.cma.2021.114132.
9. Dowson, D.; Higginson, G.R.; Whitaker, A.V. Elasto-Hydrodynamic Lubrication: A Survey of Isothermal Solutions. *Journal of Mechanical Engineering Science* **1962**, *4*, 121–126. https://doi.org/10.1243/jmes_jour_1962_004_018_02.
10. Moes, H. Discussion on Paper D1 by D. Dowson. *Proc Instn Mech Engrs* **1966**, *180*, 244–245.
11. Paouris, L.; Rahmani, R.; Theodossiades, S.; Rahnejat, H.; Hunt, G.; Barton, W. An Analytical Approach for Prediction of Elastohydrodynamic Friction with Inlet Shear Heating and Starvation. *Tribology Letters* **2016**, *64*. https://doi.org/10.1007/s11249-016-0740-5.
12. Habchi, W.; Bair, S.; Qureshi, F.; Covitch, M. A Film Thickness Correction Formula for Double-Newtonian Shear-Thinning in Rolling EHL Circular Contacts. *Tribology Letters* **2012**, *50*, 59–66. https://doi.org/10.1007/s11249-012-0078-6.
13. Habchi, W.; Bair, S. Quantitative Compressibility Effects in Thermal Elastohydrodynamic Circular Contacts. *Journal of Tribology* **2012**, *135*. https://doi.org/10.1115/1.4023082.
14. Gupta, P.K.; Cheng, H.S.; Zhu, D.; Forster, N.H.; Schrand, J.B. Viscoelastic Effects in MIL-L-7808-Type Lubricant, Part I: Analytical Formulation. *Tribology Transactions* **1992**, *35*, 269–274. https://doi.org/10.1080/10402009208982117.
15. Houpert, L. Ball Bearing and Tapered Roller Bearing Torque: Analytical, Numerical and Experimental Results. *Tribology Transactions* **2002**, *45*, 345–353. https://doi.org/10.1080/10402000208982559.
16. Manjunath, M.; Fauconnier, D.; Ost, W.; De Baets, P. Experimental Analysis of Rolling Torque and Thermal Inlet Shear Heating in Tapered Roller Bearings. *Machines* **2023**, *11*. https://doi.org/10.3390/machines11080801.
17. Habchi, W.; Bair, S. Machine-Learning-Assisted Identification and Formulation of High-Pressure Lubricant-Piezoviscous-Response Parameters for Minimum Film Thickness Determination in Elastohydrodynamic Circular Contacts. *Tribology Letters* **2024**, *72*. https://doi.org/10.1007/s11249-024-01937-2.
18. Walker, J.; Questa, H.; Raman, A.; Ahmed, M.; Mohammadpour, M.; Bewsher, S.R.; Offner, G. Application of Tribological Artificial Neural Networks in Machine Elements. *Tribology Letters* **2022**, *71*. https://doi.org/10.1007/s11249-022-01673-5.
19. Singh, A.; Wolf, M.; Jacobs, G.; König, F. Machine learning based surrogate modelling for the prediction of maximum contact temperature in EHL line contacts. *Tribology International* **2023**, *179*, 108166. https://doi.org/10.1016/j.triboint.2022.108166.
20. Tošić, M.; Marian, M.; Habchi, W.; Lohner, T.; Stahl, K. Application of machine learning for film thickness prediction in elliptical EHL contact with varying entrainment angle. *Tribology International* **2024**, *199*, 109940. https://doi.org/https://doi.org/10.1016/j.triboint.2024.109940.
21. Kelley, J.; Schneider, V.; Poll, G.; Marian, M. Enhancing practical modeling: A neural network approach for locally-resolved prediction of elastohydrodynamic line contacts. *Tribology International* **2024**, *199*, 109988. https://doi.org/https://doi.org/10.1016/j.triboint.2024.109988.
22. Habchi, W. *Finite element modeling of elastohydrodynamic lubrication problems*; John Wiley & Sons, 2018.
23. Gohar, R. *Elastohydrodynamics*; World Scientific, 2001.
24. Ardah, S.; Profito, F.J.; Dini, D. An integrated finite volume framework for thermal elasto-hydrodynamic lubrication. *Tribology International* **2023**, *177*, 107935. https://doi.org/10.1016/j.triboint.2022.107935.
25. Kim, H.J.; Ehret, P.; Dowson, D.; Taylor, C.M. Thermal elastohydrodynamic analysis of circular contacts part 1: Newtonian model. *Proceedings of the Institution of Mechanical Engineers, Part J: Journal of Engineering Tribology* **2001**, *215*, 339–352.
26. Carslaw, H.S.; Jaeger, J. Conduction of heat in solids: Oxford University Press. *New York* **1959**, p. 510.
27. Houpert, L. New Results of Traction Force Calculations in Elastohydrodynamic Contacts. *Journal of Tribology* **1985**, *107*, 241–245, [https://asmedigitalcollection.asme.org/tribology/article-pdf/107/2/241/5746893/241_1.pdf]. https://doi.org/10.1115/1.3261033.
28. Habchi, W.; Vergne, P.; Bair, S.; Andersson, O.; Eyheramendy, D.; Morales-Espejel, G. Influence of pressure and temperature dependence of thermal properties of a lubricant on the behaviour of circular TEHD contacts. *Tribology International* **2010**, *43*, 1842–1850. 36th Leeds–Lyon Symposium Special Issue: Multi-facets of Tribology, https://doi.org/https://doi.org/10.1016/j.triboint.2009.10.002.

29. Liu, S.; Qiu, L.; Wang, Z.; Chen, X. Influences of Iteration Details on Flow Continuities of Numerical Solutions to Isothermal Elastohydrodynamic Lubrication With Micro-Cavitations. *Journal of Tribology* **2021**, *143*. https://doi.org/10.1115/1.4049327.
30. Dalcin, L.D.; Paz, R.R.; Kler, P.A.; Cosimo, A. Parallel distributed computing using Python. *Advances in Water Resources* **2011**, *34*, 1124–1139. https://doi.org/10.1016/j.advwatres.2011.04.013.
31. Balay, S.; Abhyankar, S.; Adams, M.; Brown, J.; Brune, P.; Buschelman, K.; Constantinescu, E.; Dener, A.; Faibussowitsch, J.; Gropp, W.; et al. *PETSc/TAO Users Manual Revision 3.22*; 2024. https://doi.org/10.2172/2476320.
32. Wang, Q.J.; Zhu, D. Interfacial Mechanics: Theories and Methods for Contact and Lubrication, 2019. https://doi.org/10.1201/9780429131011.
33. Degroote, J.; Bruggeman, P.; Haelterman, R.; Vierendeels, J.; Degroote, J.; Bruggeman, P.; Haelterman, R.; Vierendeels, J. Stability of a coupling technique for partitioned solvers in FSI applications. *Computers & Structures* **2008**, *86*, 2224–2234. https://doi.org/https://doi.org/10.1016/j.compstruc.2008.05.005.
34. Akiba, T.; Sano, S.; Yanase, T.; Ohta, T.; Koyama, M. Optuna: A Next-generation Hyperparameter Optimization Framework. In Proceedings of the Proceedings of the 25th ACM SIGKDD International Conference on Knowledge Discovery and Data Mining, 2019.
35. Liu, F.T.; Ting, K.M.; Zhou, Z.H. Isolation Forest. In Proceedings of the 2008 Eighth IEEE International Conference on Data Mining. IEEE, 2008, pp. 413–422. https://doi.org/10.1109/icdm.2008.17.
36. Breunig, M.M.; Kriegel, H.P.; Ng, R.T.; Sander, J. LOF: identifying density-based local outliers. In Proceedings of the Proceedings of the 2000 ACM SIGMOD international conference on Management of data. ACM, 2000, SIGMOD/PODS00, pp. 93–104. https://doi.org/10.1145/342009.335388.
37. Lundberg, S.M.; Lee, S.I. A Unified Approach to Interpreting Model Predictions. In Proceedings of the Advances in Neural Information Processing Systems; Guyon, I.; Luxburg, U.V.; Bengio, S.; Wallach, H.; Fergus, R.; Vishwanathan, S.; Garnett, R., Eds. Curran Associates, Inc., 2017, Vol. 30.
38. Habchi, W.; Sperka, P.; Bair, S. Is Elastohydrodynamic Minimum Film Thickness Truly Governed by Inlet Rheology? *Tribol Lett* **2023**, *71*, 96. https://doi.org/10.1007/s11249-023-01771-y.
39. Habchi, W.; Vergne, P. On the compressive heating/cooling mechanism in thermal elastohydrodynamic lubricated contacts. *Tribology International* **2015**, *88*, 143–152. https://doi.org/https://doi.org/10.1016/j.triboint.2015.03.025.
40. Ansel, J.; Yang, E.; He, H.; Gimelshein, N.; Jain, A.; Voznesensky, M.; Bao, B.; Bell, P.; Berard, D.; Burovski, E.; et al. PyTorch 2: Faster Machine Learning Through Dynamic Python Bytecode Transformation and Graph Compilation. In Proceedings of the 29th ACM International Conference on Architectural Support for Programming Languages and Operating Systems, Volume 2 (ASPLOS '24). ACM, 2024. https://doi.org/10.1145/3620665.3640366.
41. Yeo, I.; Johnson, R.A. A new family of power transformations to improve normality or symmetry. *Biometrika* **2000**, *87*, 954–959, [https://academic.oup.com/biomet/article-pdf/87/4/954/633221/870954.pdf]. https://doi.org/10.1093/biomet/87.4.954.